



Molecular adsorption promotes carrier migration: Key step for molecular oxygen activation of defective $\text{Bi}_4\text{O}_5\text{I}_2$

Xiaoli Jin, Chade Lv, Xin Zhou*, Congmin Zhang, Qingqiang Meng, Yue Liu, Gang Chen*

MIIT Key Laboratory of Critical Materials Technology for New Energy Conversion and Storage, School of Chemistry and Chemical Engineering, Harbin Institute of Technology, Harbin, PR China



ARTICLE INFO

Keywords:

Oxygen vacancies
 $\text{Bi}_4\text{O}_5\text{I}_2$
 Molecular adsorption
 Carrier migration
 Molecular oxygen activation

ABSTRACT

Oxide defect engineering in semiconductors is of growing interest and considered as an important strategy for promoting photocatalytic performance, as it enables to couple solar energy into oxygen activation. Herein, the surface oxygen vacancies are introduced into bismuth-rich $\text{Bi}_4\text{O}_5\text{I}_2$ nanosheets ($\text{Bi}_4\text{O}_5\text{I}_2\text{-OV}$) via a facile solvothermal route. By introducing oxygen vacancies into $\text{Bi}_4\text{O}_5\text{I}_2$, the molecule oxygen adsorption is significantly improved. More importantly, attributed to the molecular oxygen adsorption, an instantaneous surface-bulk homojunction is constructed, which facilitates the separation and transport of photogenerated charge carriers. Therefore, noticeable molecular oxygen activation and N_2 fixation are achieved in $\text{Bi}_4\text{O}_5\text{I}_2\text{-OV}$. These findings may shed light on designing highly efficient photocatalysts and provide fresh insights into understanding the charge migration mechanism in oxygen vacancies-related photocatalytic system.

1. Introduction

Photocatalytic technology is considered as one of the most green and sustainable technologies to control environmental pollution in recent years due to its potential applications for environmental remediation [1]. It is well established that molecular oxygen activation plays a vital role in photocatalytic degradation of organic contaminants, because the effective capture of electrons by molecular oxygen is capable of suppressing the recombination of photo-induced electron-hole pairs and the generated reactive oxygen species (ROS) are active initiators of pollution degradation [2–11]. Therefore, it is of great significance to enhance molecular oxygen activation for achieving excellent photocatalytic activity.

It has been proved by previous reports that molecular oxygen adsorption on the surface of semiconductors is an essential prerequisite for molecular oxygen activation, and the activation pathway depends greatly on the adsorbing capacity of molecular oxygen [12–15]. It is widely accepted that the surface oxygen vacancies of materials are usually serving as adsorption sites of the molecular oxygen, while a clean surface usually has weak affinity to molecular oxygen [16]. Therefore, the introduction of oxygen vacancies into materials is regarded as an effect way to promote molecular oxygen activation. Recently Xie et al. reported that the hetero-layered inorganic semiconductors possess considerable electron–hole interactions which could favor the photocatalytic molecular oxygen activation behaviors [17]. As

a class of typical layer-structured photocatalysts, BiOX ($\text{X} = \text{Cl}, \text{Br}, \text{I}$) possess unique structures which can provide a large enough space to polarize related atoms and orbitals, endowing oxygen vacancies easily formed under the external force. For instance, under UV light irradiation, black BiOCl with oxygen vacancies was prepared and the amount of ROS increased with the irradiation time prolonged [18].

The bismuth-rich $\text{Bi}_x\text{O}_y\text{X}_z$ ($\text{X} = \text{Cl}, \text{Br}, \text{I}$) photocatalytic materials have similar layered structure with BiOX . In recent years, various works have confirmed that $\text{Bi}_x\text{O}_y\text{X}_z$ display higher photocatalytic activity than BiOX in general due to their efficient photon absorption and charge separation [19–24]. For example, benefiting from the efficient visible light absorption, $\text{Bi}_{12}\text{O}_{17}\text{Cl}_2$ exhibited a drastically enhanced visible-light photoreactivity for degradation of bisphenol A [25]. $\text{Bi}_{24}\text{O}_{31}\text{Br}_{10}$ presented the highest activity among Bi_2O_3 , BiOBr , and $\text{Bi}_{24}\text{O}_{31}\text{Br}_{10}$ in photoreduction of water and Cr(VI) [26]. Similarly, pure $\text{Bi}_x\text{O}_y\text{X}_z$ photocatalysts ($\text{Bi}_3\text{O}_4\text{Br}$, $\text{Bi}_5\text{O}_7\text{Br}$, $\text{Bi}_5\text{O}_7\text{I}$ and $\text{Bi}_{24}\text{O}_{31}\text{Cl}_{10}$) have also been reported exhibiting superior performance towards molecular oxygen activation [27–29]. It is then supposed reasonable to conjecture that high-efficient $\text{Bi}_x\text{O}_y\text{X}_z$ photocatalysts for molecular oxygen activation would be achieved by introducing surface oxygen vacancies to promote the adsorption. Nevertheless, to the best of our knowledge, the oxygen vacancies engineered $\text{Bi}_x\text{O}_y\text{X}_z$ are rarely reported. Moreover, most researches on molecular oxygen activation are mainly concentrated on surface adsorption, whereas the investigation on electron migration during the activation process is overlooked, which is another decisive

* Corresponding authors.

E-mail addresses: zhoux@hit.edu.cn (X. Zhou), gchen@hit.edu.cn (G. Chen).

factor for molecular oxygen activation. Therefore, it is extremely essential to inquire into the interaction between molecular oxygen activation and surface properties of $\text{Bi}_x\text{O}_y\text{X}_z$ semiconductors.

In this study, we employed bismuth-rich $\text{Bi}_4\text{O}_5\text{I}_2$ nanosheets as a model material to study the interaction between surface oxygen vacancies and photocatalytic activities. $\text{Bi}_4\text{O}_5\text{I}_2$ nanosheets with oxygen vacancies (denoted as $\text{Bi}_4\text{O}_5\text{I}_2\text{-OV}$) were synthesized via a facile solvothermal method. The theoretical calculation results showed that the adsorption energy of molecular oxygen increased after forming an oxygen vacancy on the surface of $\text{Bi}_4\text{O}_5\text{I}_2$. As a result of strong O_2 adsorption on the surface, an instantaneous surface-bulk homogeneous junction was constructed, which was confirmed by the density of states (DOS) analysis. The homojunction facilitated the separation and transport of photoinduced charge carriers at the interface of surface and bulk. Ascribed to the strong O_2 adsorption and efficient charges migration, $\text{Bi}_4\text{O}_5\text{I}_2\text{-OV}$ displayed highly efficient photocatalytic molecular oxygen activation. The identical results of photocatalytic N_2 fixation was obtained over $\text{Bi}_4\text{O}_5\text{I}_2\text{-OV}$ by replacing N_2 with O_2 , showing the generality of the proposed charge migration mechanism.

2. Experimental

2.1. Materials

$\text{Bi}(\text{NO}_3)_3\cdot 5\text{H}_2\text{O}$, KI, ethanol, ethylene glycol, nitroblue tetrazolium (NBT), NaOH, isopropanol (IPA) and Ness's reagent were purchased from Aladdin Chemical Co., Ltd., which were of analytic grade and used without further purification.

2.2. Synthesis

$\text{Bi}_4\text{O}_5\text{I}_2\text{-OV}$: For the syntheses of $\text{Bi}_4\text{O}_5\text{I}_2$ nanosheets with oxygen vacancies ($\text{Bi}_4\text{O}_5\text{I}_2\text{-OV}$), 0.97 g $\text{Bi}(\text{NO}_3)_3\cdot 5\text{H}_2\text{O}$ (2 mmol) was dissolved into 10 mL ethylene glycol and 0.166 g KI (1 mmol) was dissolved into 30 mL ethanol at room temperature with continuous stirring. Then KI solution was drop-wise added into the $\text{Bi}(\text{NO}_3)_3\cdot 5\text{H}_2\text{O}$ solution under magnetic stirring for 30 min. The mixture was then transferred into 50 mL Teflon-lined stainless steel autoclaves filled up to 80% of the total volume and maintained at 160 °C for 16 h. After cooling to room temperature, the obtained black powder was collected by centrifugation, then washed with water and ethanol three times to remove residual ions and finally dried at 80 °C in air.

$\text{Bi}_4\text{O}_5\text{I}_2$: For comparison, the counterpart sample of pure $\text{Bi}_4\text{O}_5\text{I}_2$ (denoted as $\text{Bi}_4\text{O}_5\text{I}_2$) was synthesized by heating $\text{Bi}_4\text{O}_5\text{I}_2\text{-OV}$ at 200 °C in air for 3 h to reoxidize the surface which yielded yellow powder. The intermediate concentration of oxygen vacancies is acquired by regulating the heat treatment time to 1 h and 2 h, respectively. They are denoted as $\text{Bi}_4\text{O}_5\text{I}_2\text{-OV-1}$ and $\text{Bi}_4\text{O}_5\text{I}_2\text{-OV-2}$, respectively.

2.3. Characterization

The phase and crystal structure of the samples were characterized by X ray diffraction (XRD) on a Rigaku D/max-2000 diffractometer at room temperature with Cu-K α radiation ($\lambda = 0.15406 \text{ nm}$) and the 2 θ ranges from 10° to 80° at a scan rate of 4° min $^{-1}$. A Renishaw via micro-Raman spectroscopy system in the backscattering geometry with a 458 nm laser excitation was used to record the Raman spectra of samples. Their morphology was inspected with scanning electron microscope (SEM, HELIOS, 600i), transmission electron microscopy (TEM) and high-resolution transmission electron microscopy (HRTEM) which was obtained by FEI Tecnai G2S-Twin with operating at an accelerating voltage of 300 kV. UV-vis diffuse reflectance spectra (DRS) were acquired by a spectrophotometer (HITACHI UH-4150) with BaSO_4 as a reference. X-ray photoelectron spectroscopy (XPS) measurements were performed on a Thermo Scientific ESCALAB 250Xi X-ray photoelectron spectrometer with a pass energy of 20.00 eV and an excitation source of

Al K $\alpha = 1486.6 \text{ eV}$. The peak positions were corrected against the contaminated carbon C 1s peak (284.6 eV). Photoluminescence (PL) spectroscopy of the samples were accomplished using a Fluorescence Spectrophotometer (HORIBA FluoroMax-4) at room temperature ($\lambda_{\text{exc}} = 420 \text{ nm}$). Electron paramagnetic resonance (EPR) spectra were conducted on a Bruker A200 EPR Spectrometer operating at room temperature with micro frequency at 9.86 GHz.

2.4. Photocatalytic properties for molecular oxygen activation

All the visible-light photocatalytic activity experiments on the as-prepared samples were conducted at ambient temperature using a 300 W high pressure xenon lamp (Trusttech PLS-SXE 300, Beijing) with a cutoff filter ($\lambda \geq 400 \text{ nm}$). The photocatalytic activities for molecular oxygen activation were evaluated with the amount of superoxide anion radicals ($\text{O}_2^{\cdot -}$) during the photocatalytic process which was determined by nitrotetrazolium blue chloride (NBT, $1.25 \times 10^{-5} \text{ mol/L}$). NBT exhibits an absorption maximum at 265 nm, which can be detected by UV-vis spectrophotometer, however, the product of $\text{O}_2^{\cdot -}$ with NBT does not [30]. Typical photocatalytic process was arranged in this way: 0.02 g of the as-prepared sample was added into 100 mL aqueous suspension of NBT solution in a quartz beaker. Prior to irradiation, the suspensions were dispersed in the solution with an ultrasonic bath for 20 min and then were continuously stirred in dark for 30 min to reach adsorption-desorption equilibrium. The suspensions were kept under constant air-equilibrated conditions equipped with a vigorous magnetic stirring during irradiation. At the given time intervals, the photocatalyst was removed by centrifugation and the upper clear liquid of NBT solution was detected with the UV-vis spectrometer (HITACHI UH-5300).

2.5. Photocatalytic N_2 fixation

The methods of photocatalytic N_2 fixation were similar with previous reports [31]. Typically, 0.02 g of product was uniformly dispersed into 100 mL of distilled water containing 100 μL of IPA as holes scavenger at room temperature. The solution was continuously stirred in dark with high-purity N_2 bubbled for 30 min and then was irradiated under visible light irradiation. At each time interval, 5 mL of mixture was taken out and followed by centrifugation to remove the photocatalyst. The concentration of ammonia was spectrophotometrically determined by UV-vis spectrometry using Nessler's reagent as a chromogenic agent at 420 nm.

2.6. Photoelectrochemical measurement

The photocurrent behaviors and electrochemical impedance spectra (EIS) of $\text{Bi}_4\text{O}_5\text{I}_2\text{-OV}$ and $\text{Bi}_4\text{O}_5\text{I}_2$ were investigated on a AUTOLAB-PGSTAT302N electrochemical working station in a standard three-electrode electrochemical cell with Na_2SO_4 (0.5 M) electrolyte solution. A 300 W Xe light with a filter ($\lambda > 400 \text{ nm}$) was employed as the light source. FTO glass with coated photocatalysts was used as the working electrode. A Pt pole and an Ag/AgCl electrode served as the counter and reference electrode, respectively. The working electrodes were fabricated by depositing slurry containing 0.02 g photocatalyst and 300 μL terpineol on FTO glass by the spin coater. The mixture was subsequently dried at 80 °C overnight to make the materials firmly anchored to the surface. Photoelectrochemical measurement of $\text{Bi}_4\text{O}_5\text{I}_2\text{-OV}$ in O_2 and Ar conditions were carried out in O_2 and Ar-bubbling Na_2SO_4 solution, respectively.

2.7. DFT theoretical calculation

The calculations of both the bulk $\text{Bi}_4\text{O}_5\text{I}_2$ and $\text{Bi}_4\text{O}_5\text{I}_2\text{-OV}$ (10I) surface were performed by Spin-polarized density functional theory (DFT) simulations with the Vienna ab initio simulation (VASP) package.

Perdew-Burke-Ernzerhof (PBE) exchange-correlation functional within a generalized gradient approximation (GGA) and the projector augmented-wave (PAW) potential were employed with an energy cutoff of 500 eV for the plane-wave expansion [32–34]. The calculated lattice parameters are $a = 17.22$, $b = 17.18$, $c = 28.00$ Å, and $\alpha = \beta = \gamma = 90^\circ$. Oxygen vacancy was modeled by removing one oxygen atom from a unit cell. In order to simulate the molecular oxygen activation on surfaces, vacuum space of 18 Å was used to avoid the possible interaction between the unit cell and their images. In the optimization procedure, the force and energy converged to 10^{-2} eV/atom and 10^{-5} eV/Å, respectively. The k -points were set to $3 \times 3 \times 1$ for the structure relaxation and increased to $6 \times 6 \times 1$ for the electronic structure calculations. The charge analysis between the adsorbents and surface was performed by the Bader charge population. Adsorption energy was defined as:

$$E_{\text{ads}} = E_{(\text{oxygen} + \text{surface})} - E_{(\text{oxygen})} - E_{(\text{surface})}$$

where $E_{(\text{oxygen} + \text{surface})}$ was the total energy of the $\text{Bi}_4\text{O}_5\text{I}_2\text{-OV}$ ($10\bar{1}$) surface with oxygen adsorbed, and $E_{(\text{oxygen})}$ and $E_{(\text{surface})}$ were the total energy of oxygen and $\text{Bi}_4\text{O}_5\text{I}_2\text{-OV}$ ($10\bar{1}$), respectively.

3. Results and discussion

A simple solvothermal strategy using ethylene glycol and ethanol as the mixed solvents was used to fabricate the oxygen vacancies (OVs) on $\text{Bi}_4\text{O}_5\text{I}_2$ nanosheets. The possible formation process was illustrated in Fig. 1a. As reported, ethylene glycol could reduce the surface oxygen atoms of BiOX to generate OVs on the high oxygen density of $\{001\}$ facets [35]. Owing to the very similar structure with BiOX, ethylene glycol molecules may serve the same function during the formation of OVs on $\text{Bi}_x\text{O}_y\text{X}_z$. In the case of $\text{Bi}_4\text{O}_5\text{I}_2$, the facets of high oxygen density was considered as $\{10\bar{1}\}$ facets and the internal electric field was also along the $[10\bar{1}]$ direction which was helpful for the photoinduced charge separation. During the solvothermal synthesis, ethylene glycol molecules could react with surface oxygen atoms to remove surface oxygen, leaving oxygen vacancies on the $\{10\bar{1}\}$ facet of $\text{Bi}_4\text{O}_5\text{I}_2$. Then

$\text{Bi}_4\text{O}_5\text{I}_2$ was obtained by heating of $\text{Bi}_4\text{O}_5\text{I}_2\text{-OV}$ at 200 °C in air atmosphere for 3 h to eliminate the defects.

XRD patterns were used to determine the crystal phase and composition information of the as-synthesized samples. Since there was no standard JCPDS card corresponding to the characteristic peaks of $\text{Bi}_4\text{O}_5\text{I}_2$, the peaks at 24.2°, 28.8°, 31.7°, 45.7°, 54.9° matched well with the monoclinic phase (space group: P21, unit cell parameters: $a = 1.494$ nm, $b = 0.5698$ nm, and $c = 1.126$ nm, $a = c = 90.0$, $b = 99.8$) of $\text{Bi}_4\text{O}_5\text{I}_2$ reported by Keller et al. (Fig. 1b) [36]. The results were also in agreement with previous XRD study of $\text{Bi}_4\text{O}_5\text{I}_2$ [37,38]. SEM image (Fig. 1c) depicted a nanosheets morphology of $\text{Bi}_4\text{O}_5\text{I}_2\text{-OV}$. In addition, the crystal phase and morphology of $\text{Bi}_4\text{O}_5\text{I}_2\text{-OV}$ after oxygen backfill had no significant changes (Fig. S1).

A deeper insight into the detailed structures of $\text{Bi}_4\text{O}_5\text{I}_2\text{-OV}$ sample was acquired by transmission electron microscopy (TEM) and high-resolution transmission electron microscopy (HRTEM) images. As presented in Fig. 2a and b, the thickness of as-synthesized $\text{Bi}_4\text{O}_5\text{I}_2\text{-OV}$ ultrathin nanosheets was about 5 nm. According to the crystal structure of $\text{Bi}_4\text{O}_5\text{I}_2$, the dominant exposed facets were $\{10\bar{1}\}$ facets, which were also proved by HRTEM and fast-fourier transform (FFT) images. As shown in Fig. 2c, HRTEM image of $\text{Bi}_4\text{O}_5\text{I}_2\text{-OV}$ nanosheets with side orientation revealed the characteristic spacing of 0.97 nm for the $\{10\bar{1}\}$ lattice planes of $\text{Bi}_4\text{O}_5\text{I}_2$. The enlarged HRTEM image and corresponding FFT pattern with top orientation of the nanosheet were presented in Fig. 2d. Two clear lattice fringes with interplanar lattice spacing of 0.27 nm and 0.284 nm corresponded to the $\{303\}$ and $\{020\}$ facets of $\text{Bi}_4\text{O}_5\text{I}_2$, respectively. The angle between $\{303\}$ and $\{020\}$ facets was 90°, which agreed well with theoretical angle (90°) and the corresponding FFT pattern showed the angle between $\{323\}$ and $\{020\}$ facets was 46.06°, which also matched with the theoretical angles (46.13°). Based on the above analysis, it could be concluded that the $\text{Bi}_4\text{O}_5\text{I}_2\text{-OV}$ was ultra-thin single crystal nanosheets with about 5–8 atom layers and was enclosed by $\{10\bar{1}\}$ facets. Fig. 2e and f exhibited the atomic structure of $\text{Bi}_4\text{O}_5\text{I}_2$ exposing $\{10\bar{1}\}$ facet with side view and top view, respectively. Besides, there is nearly no amorphous product observed from the margin of the HRTEM image, indicating its good

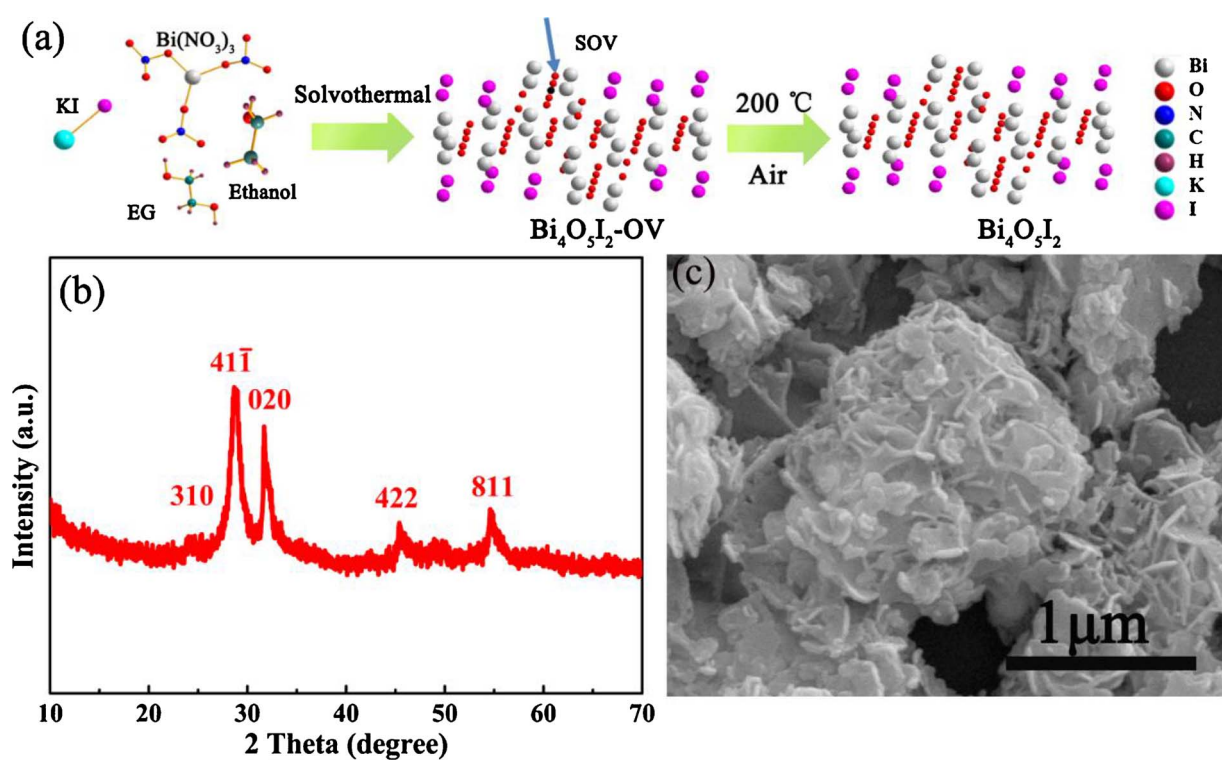


Fig. 1. Schematic illustration of synthesis process (a), XRD pattern (b) and SEM image (c) of the as-synthesized $\text{Bi}_4\text{O}_5\text{I}_2\text{-OV}$.

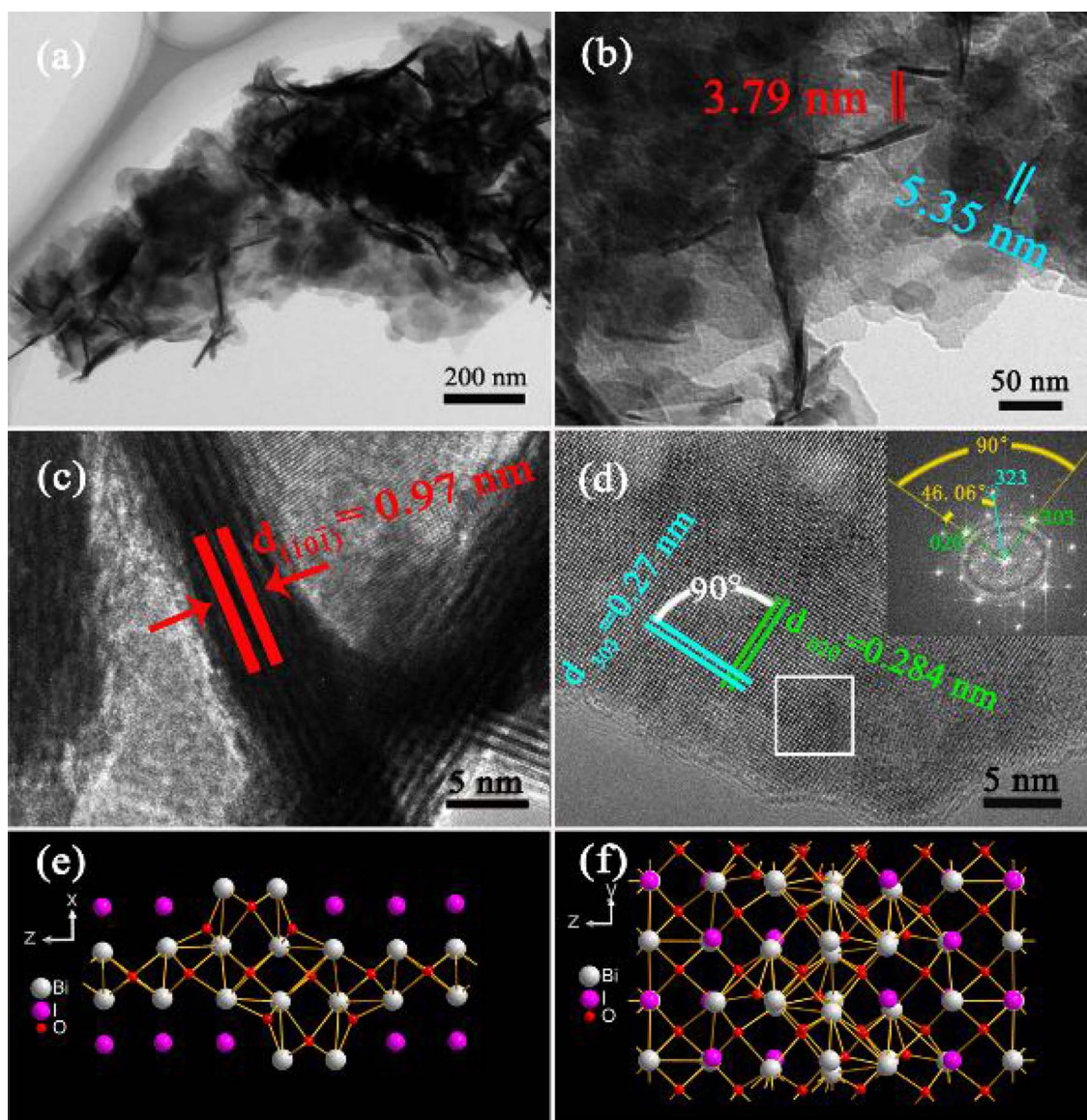


Fig. 2. TEM images of $\text{Bi}_4\text{O}_5\text{I}_2\text{-OV}$ (a and b), HRTEM images of $\text{Bi}_4\text{O}_5\text{I}_2\text{-OV}$ nanosheets with side view (c) and top view (d), atomic structure of $\{10\bar{1}\}$ facet with side view (e) and top view (f). (The insert image is the corresponding FFT pattern of red range in d).

crystallinity. The loose bond energy around oxygen atoms in high oxygen density of $\{10\bar{1}\}$ facet made it easy to lose oxygen atoms, leaving OVs on the surface.

To verify the presence of oxygen vacancies, the electron paramagnetic resonance (EPR) technique was applied. Low-temperature EPR analysis (Fig. 3a) showed a typical signal of oxygen vacancies at $g = 2.001$ [39,40]. On the contrary, there was no EPR signal for $\text{Bi}_4\text{O}_5\text{I}_2$. It indicated that oxygen vacancies were successfully formed via the solvothermal method. The existence of oxygen vacancies could cause the distinct coordination of oxygen species, which was confirmed by the O 1s XPS (Fig. 3b). Prior to heat treatment, the O 1s characteristic peaks of $\text{Bi}_4\text{O}_5\text{I}_2\text{-OV}$ were deconvoluted into three main peaks of low, medium, and high binding energy peaks at 529.0, 530.0 and 531.1 eV, respectively. The medium binding energy peak was corresponding to oxygen vacancies, and the low and high binding energy peaks were associated with the lattice oxygen and surface hydroxyl groups, respectively [41]. After the heat treatment, the peak of O 1s around 530.0 eV from $\text{Bi}_4\text{O}_5\text{I}_2$ could not be observed, indicating that oxygen vacancy sites of the $\text{Bi}_4\text{O}_5\text{I}_2$ had been filled up by O_2 .

The introduction of vacancies was supposed to induce indirect subbands excitation to enhance the optical absorption properties [42]. As

determined from UV-vis diffuse reflectance spectra (Fig. 3c), a continuous and exponentially decaying absorption tails across the whole light region with slight band edge shifting appeared, indicating the extended light absorption of $\text{Bi}_4\text{O}_5\text{I}_2\text{-OV}$. This was also reflected by the colors of samples: black color of $\text{Bi}_4\text{O}_5\text{I}_2\text{-OV}$, which was different from the yellow color of $\text{Bi}_4\text{O}_5\text{I}_2$. It should be noted that the organic substances during high-temperature hydrothermal system can work as the reducing agent, which possibly causes the formation of reduced $\text{Bi}_4\text{O}_5\text{I}_2$ or carbon, showing a black color. As a result, Raman spectra of $\text{Bi}_4\text{O}_5\text{I}_2\text{-OV}$ and $\text{Bi}_4\text{O}_5\text{I}_2$ have been conducted to eliminate the possible carbon allotropes, as shown in Fig. S2. Because $\text{Bi}_4\text{O}_5\text{I}_2$ was an indirect excitation photocatalyst, the band gap (E_g) could be calculated by the plot of $(ahv)^{1/2}$ versus energy ($h\nu$) as shown in Fig. 3d [19]. The estimated E_g of $\text{Bi}_4\text{O}_5\text{I}_2\text{-OV}$ and $\text{Bi}_4\text{O}_5\text{I}_2$ were about 2.04 eV and 2.44 eV, respectively. The valence-band XPS spectra (Fig. 3e) showed that the valence band positions of the samples had no obvious changes. According to the empirical equations:

$$E_{\text{VBM}} = E_{\text{CBM}} + E_g$$

where E_{VBM} and E_{CBM} were the valence band maximum position and conduction band minimum position, respectively. Therefore, the

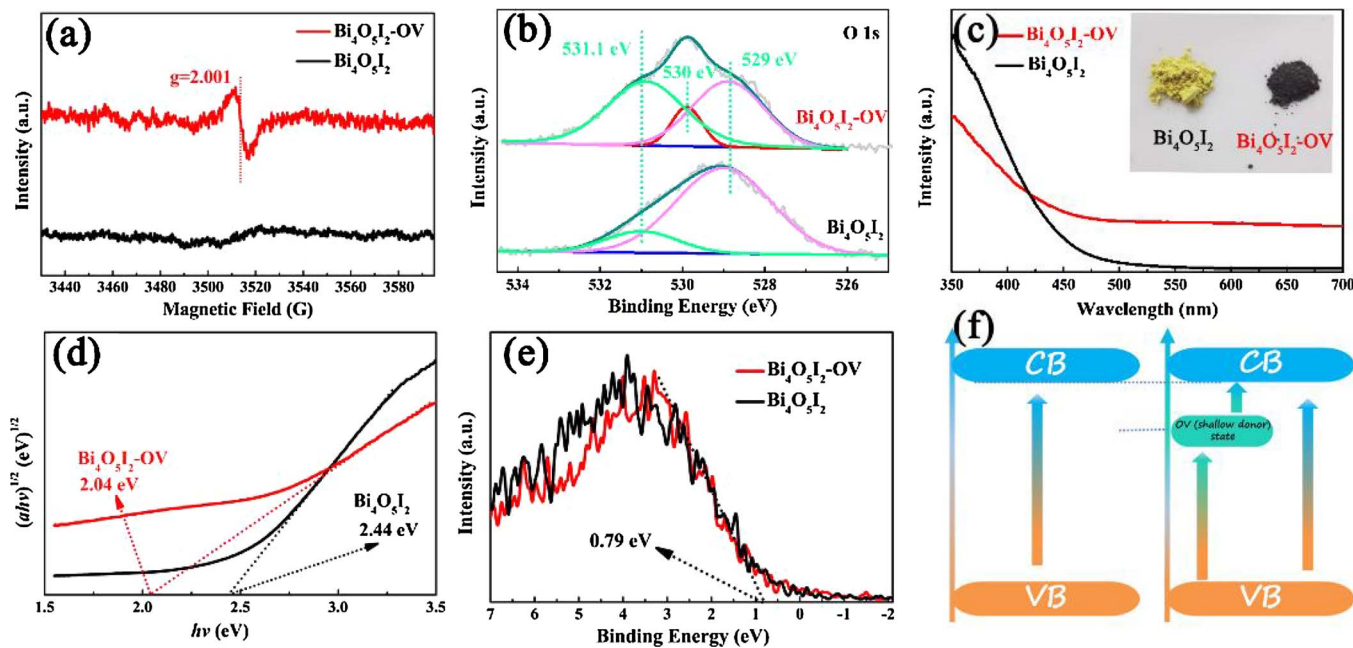


Fig. 3. Room-temperature EPR spectra (a), High-resolution O 1s XPS spectra (b), UV-vis diffuse reflectance spectra (c), the plots of $(ah\nu)^{1/2}$ vs. photon energy ($h\nu$) (d), valence-band XPS spectra (e) and the schematics illustrating the electronic band structures of $\text{Bi}_4\text{O}_5\text{I}_2\text{-OV}$ and $\text{Bi}_4\text{O}_5\text{I}_2$. (The inset image is the photograph of samples). (For interpretation of the references to color in this figure, the reader is referred to the web version of this article).

oxygen vacancies state which was 0.4 eV lower than the conduction band of $\text{Bi}_4\text{O}_5\text{I}_2\text{-OV}$ formed. Based on the above information, the schematics depiction of the band structures of $\text{Bi}_4\text{O}_5\text{I}_2$ samples was illustrated in Fig. 3f. Electronic transitions from VB to oxygen vacancies state, and from oxygen vacancies state to CB, were responsible for the extended light absorption of $\text{Bi}_4\text{O}_5\text{I}_2\text{-OV}$. More importantly, oxygen vacancies state below CB could act as a shallow donor state [43]. The shallow donor state was in favor of transferring electrons to O_2 adsorbed on surface.

The EPR results in combination with the XPS and DRS analysis sufficiently testified that oxygen vacancies were successfully introduced into $\text{Bi}_4\text{O}_5\text{I}_2$. In order to explore the relationship between oxygen vacancies and molecular oxygen adsorption, theoretical calculations of O_2 adsorbed on the (10̄1) surface of $\text{Bi}_4\text{O}_5\text{I}_2$ and $\text{Bi}_4\text{O}_5\text{I}_2\text{-OV}$ (denote as $\text{Bi}_4\text{O}_5\text{I}_2\text{-O}_2$ and $\text{Bi}_4\text{O}_5\text{I}_2\text{-OV-O}_2$) were further carried out. As shown in Fig. 4a, the O_2 adsorbed on the (10̄1) surface of $\text{Bi}_4\text{O}_5\text{I}_2$ with a distance of 3.129 Å and 3.466 Å between Bi and O_2 . After removing an oxygen atom from the surface (Fig. 4b), the O_2 adsorbed on the top of the oxygen vacancy and the bond lengths of Bi-O shortened to 2.916 Å and 3.166 Å, respectively. Furthermore, the adsorption energies ($E_{(\text{ads})}$) of

O_2 on the surface of $\text{Bi}_4\text{O}_5\text{I}_2$ and $\text{Bi}_4\text{O}_5\text{I}_2\text{-OV}$ were -0.16 eV and -0.39 eV. Both of the shorter distance and larger adsorption energy for the $\text{Bi}_4\text{O}_5\text{I}_2\text{-OV-O}_2$ indicated that the oxygen vacancy reinforced the O_2 adsorption. The activation of O_2 in our case could be reflected by the change of O–O bond length and number of electron transfer. It could be found that the O–O bond length of O_2 extended to 1.271 Å, which was longer than that of absorbed on the surface of $\text{Bi}_4\text{O}_5\text{I}_2$ (1.251 Å) and the standard molecular oxygen (1.21 Å). In addition, Bader charge analysis showed that the electron transferring from the surface of $\text{Bi}_4\text{O}_5\text{I}_2\text{-OV}$ to O_2 was 0.337 e, while that for $\text{Bi}_4\text{O}_5\text{I}_2$ was only 0.177 e. The elongated O–O bond and increased transferred electrons indicated that the adsorbed O_2 on the surface of $\text{Bi}_4\text{O}_5\text{I}_2\text{-OV}$ would be more easily activated. Obviously, the O_2 adsorbed on the oxygen vacancy site could be bonded to the neighboring two Bi atoms and form a complex bridge configuration that promoted more electrons transferring to the adsorbed O_2 and generated more $\text{O}_2^{\cdot-}$ species. The calculation results indicated the oxygen vacancies strengthened the O_2 adsorption and made the adsorbed O_2 easier to be activated.

The photocatalytic activity for molecular oxygen activation was evaluated by measuring the generation of the $\text{O}_2^{\cdot-}$ in aqueous solution

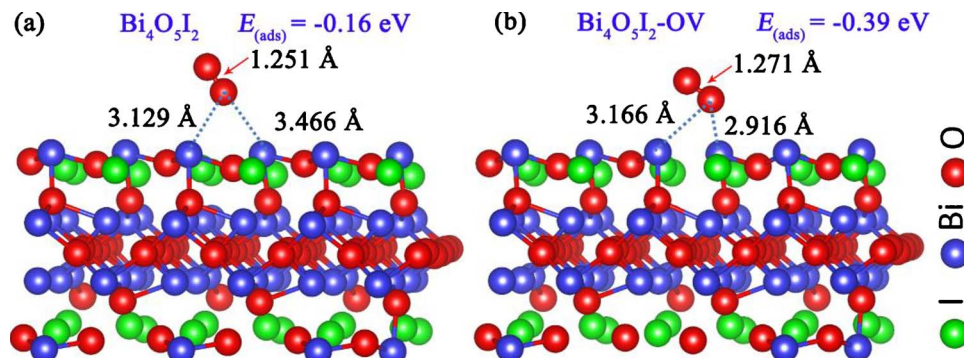


Fig. 4. Theoretical simulation the adsorption of O_2 on (10̄1) surface of $\text{Bi}_4\text{O}_5\text{I}_2\text{-OV}$ (a) and perfect (10̄1) surface of $\text{Bi}_4\text{O}_5\text{I}_2$ (b).

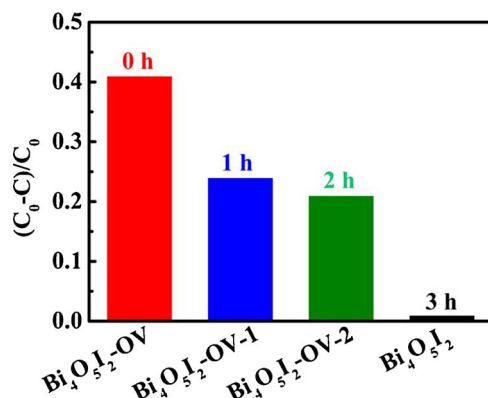


Fig. 5. Photocatalytic NBT degradation over the obtained samples after different calcination times at 200 °C.

under visible light. In this work, the production of O_2^- was quantitatively analyzed by detecting the concentration of NBT. As displayed in Fig. S4, the maximum absorbance evolution of 259 nm peak suggests the degradation of NBT with $Bi_4O_5I_2$ -OV. Whereas the concentration of NBT over $Bi_4O_5I_2$ had no obvious decrease under the same condition, signifying the very limit molecular oxygen activation of $Bi_4O_5I_2$. Additionally, no obvious O_2^- generation was detected under 500 nm monochromatic light irradiation (Fig. S5), indicating the effect of extended light absorption towards molecular oxygen activation could be ignored. Furthermore, in order to investigate the effect of oxygen vacancies concentration on the charge transfer, a series of $Bi_4O_5I_2$ with different oxygen vacancies amount were prepared by changing the heat treatment time. As the calcination time prolonged, an increasing number of oxygen vacancies are filled, resulting in a lower concentration of oxygen vacancies. The photographs and SEM images are shown in Fig. S6 and Fig. S7. Their excellent color changer confirmed that the oxygen vacancies with different concentrations are successfully achieved.

The photocatalytic NBT degradation over the obtained samples after different calcination times at 200 °C is studied as displayed in Fig. 5. It can be seen that the NBT degradation is dependent on the amount of oxygen vacancies of $Bi_4O_5I_2$. When the fresh oxygen vacancies is introduced into $Bi_4O_5I_2$, the abundant oxygen vacancies endow it possesses stronger surface oxygen adsorption and thus resulting in the improvement of carrier separation. As the number of refilled oxygen increased, the percentage degradation of NBT was decreased. This means that the concentration of oxygen vacancies and photocatalytic molecular oxygen activation were positively correlated in a certain range. Therefore, it inferred that the strengthened surface oxygen adsorption induced by oxygen vacancies was one of the primary factors that accounted for the efficient molecular oxygen activation in $Bi_4O_5I_2$ -OV.

The hydrothermal time or temperature has an important effect on the number of oxygen vacancies, resulting in a final different performance. The impact of hydrothermal time and temperature on the photocatalytic performance for molecular oxygen activation of the samples is performed under visible light by using a 400 nm cut-off filters (Fig. S8- Fig. S11). Noticeably, the samples are agglomerated into blocks with prolonging the reaction time and the strong diffraction peaks of Bi are found when the temperature raised to 200 °C. Therefore, the optimum condition of generating oxygen vacancies on $Bi_4O_5I_2$ for molecular oxygen activation is considered as using hydrothermal method at 160 °C for 16 h.

One electron or two electrons reduction generally proceed during the molecular oxygen activation, as a result, the photocatalytic molecular oxygen activation was also intensely affected by the migration and separation of photoinduced electron-hole pairs [44]. The charge transfer properties of $Bi_4O_5I_2$ samples were evaluated by photocurrent responses and the electrochemical impedance (EIS) experiments. As

shown in Fig. 6a, the low dark current density for both $Bi_4O_5I_2$ -OV and $Bi_4O_5I_2$ indicating no electron and hole were excited. When the electrodes were illuminated under visible light, the current increased due to the charge photogeneration in both samples. Noticeably, $Bi_4O_5I_2$ -OV revealed a nearly threefold enhanced photocurrent response than that of $Bi_4O_5I_2$, which inferred that the introduction of oxygen vacancies on $Bi_4O_5I_2$ could effectively promote the migration of photoinduced carriers. On the other hand, $Bi_4O_5I_2$ -OV presented an arc radius with a smaller diameter than $Bi_4O_5I_2$ (Fig. 6b), which indicated that the charge transfer resistance was remarkably decreased and thus the electronic conductivity of $Bi_4O_5I_2$ -OV was enhanced. The carrier separation had been confirmed by photoluminescence (PL) emission spectra which was a traditional tool to characterize the radiative recombination process of photoexcited carriers in a photocatalyst [45]. As shown in Fig. 6c, in contrast to the higher PL peak intensity of $Bi_4O_5I_2$, $Bi_4O_5I_2$ -OV displayed a relatively lower intensity, responding to the more efficient separation of charge carries. Moreover, the time-resolved fluorescence decay spectra (Fig. 6d) revealed the fluorescence intensities of $Bi_4O_5I_2$ and $Bi_4O_5I_2$ -OV decayed exponentially. By fitting the decay spectra, the triplet radiative lifetimes and the corresponding parameters were summarized in Table S1. The life-time of charge carriers for $Bi_4O_5I_2$ -OV was 6.85 ns, which was longer than that of $Bi_4O_5I_2$. All above results proved the migration and separation rate of the photoinduced carriers were efficaciously improved after introducing OVs in $Bi_4O_5I_2$. It has been reported some substance molecular adsorbed on the surface of material may alter the surface state, thus resulting in the improvement of carrier separation [46]. Inspired by this impacts of surface adsorption, we inferred that surface oxygen adsorption induced by oxygen vacancies might affect the surface state of $Bi_4O_5I_2$, which thereby gave rise to promoted separation and transport of charge carriers.

To confirm above viewpoint, the total density of states (DOS) and partial DOS of bulk $Bi_4O_5I_2$ and the surface of $Bi_4O_5I_2$ -OV with absorbed O_2 ($Bi_4O_5I_2$ -OV- O_2) were calculated (Fig. 7a). The DOS of bulk $Bi_4O_5I_2$ and $Bi_4O_5I_2$ -OV- O_2 were obviously different. Compared with bulk $Bi_4O_5I_2$, contribution of O_2 appears near the Fermi level and the band gap becomes narrower with the energy level of the valence band and conduction band of $Bi_4O_5I_2$ -OV- O_2 being promoted. This mismatched level might cause an instantaneous homojunction formed and thereby instantaneously developed a built-in field at the interface of $Bi_4O_5I_2$ -OV- O_2 and bulk $Bi_4O_5I_2$. The composition identity on both sides of the interface in such homojunction could give rise to a continuous band bending, which was much favorable for charge transfer across the interface and facilitated the carrier separation [47,48] (Fig. 7b). As a consequence, enhanced photocatalytic degradation activities were achieved over $Bi_4O_5I_2$ -OV (Fig. S12).

The photocurrent responses of $Bi_4O_5I_2$ -OV with O_2 or Ar atmosphere conditions were employed to provide a direct evidence to support the above charge migration mechanism involving the adsorption (Fig. 8). $Bi_4O_5I_2$ -OV with O_2 -bubbling exhibited significantly enhanced photocurrent intensity compared to that with Ar treatment. It inferred that the construction of instantaneous homojunction after O_2 adsorption on $Bi_4O_5I_2$ -OV was achieved, which resulted in the effective separation and transfer of photoinduced carriers. This might open a new insight into how surface adsorption affect charge transfer.

The above proposed mechanism suggested that the enhanced molecular oxygen activation of $Bi_4O_5I_2$ -OV was origin from the extended molecular oxygen adsorption. Hence, the generality of the proposed mechanism could be examined by the activate properties of other molecules adsorbed on $Bi_4O_5I_2$ -OV. The OVs were considered as the catalytic centers capable of adsorbing N_2 over $BiOBr$ nanosheets [49]. So in order to verify the generality of proposed mechanism, the photocatalytic N_2 fixation over $Bi_4O_5I_2$ -OV and $Bi_4O_5I_2$ samples were further conducted by replacing O_2 molecular with N_2 (Fig. 9). And the consistent results with molecular oxygen activation were obtained: $Bi_4O_5I_2$ -OV could generate a significant amount of NH_3 while no obvious NH_3 was detected in the case of pure $Bi_4O_5I_2$ under the same condition. This

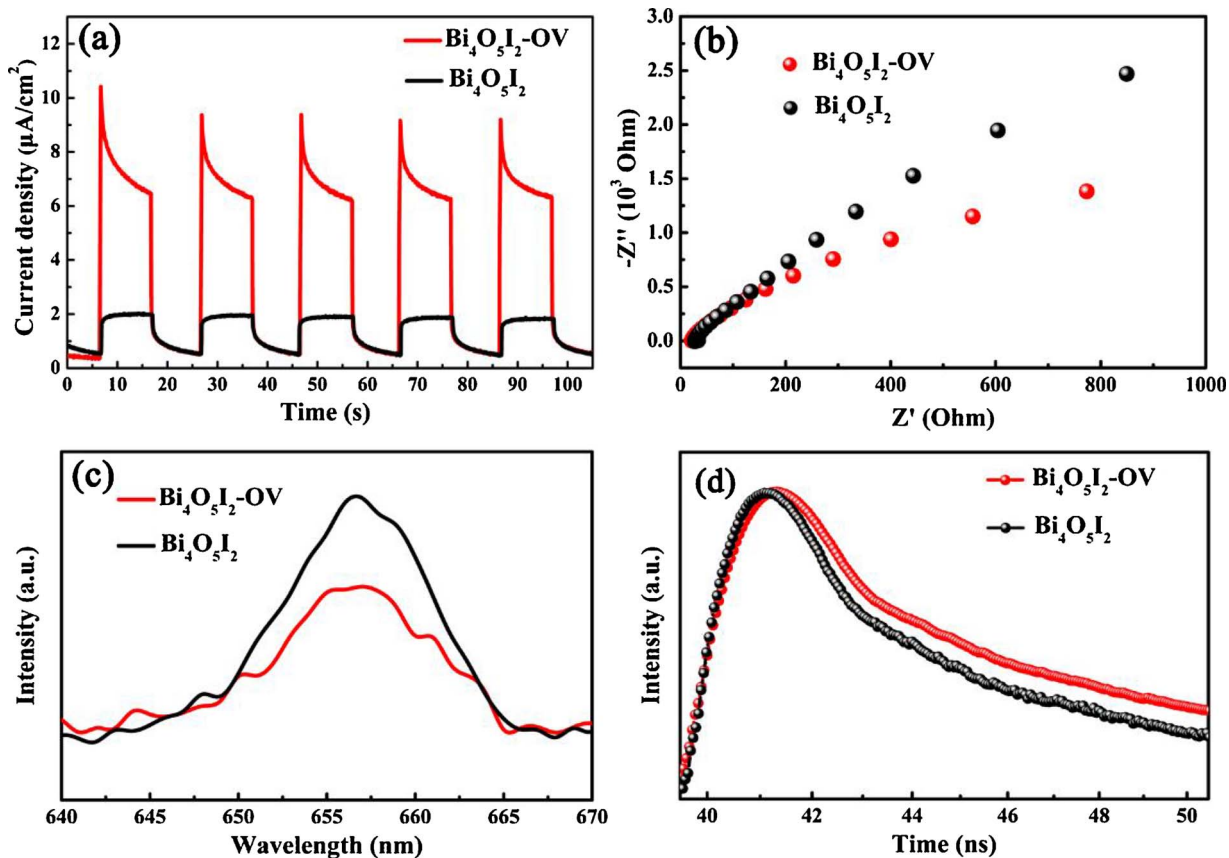


Fig. 6. Photocurrent responses (a), electrochemical impedance plots (b), PL spectra (c) and time-resolved fluorescence decay spectra (d) of $\text{Bi}_4\text{O}_5\text{I}_2\text{-OV}$ and $\text{Bi}_4\text{O}_5\text{I}_2$.

suggested that the photocatalytic N_2 fixation of $\text{Bi}_4\text{O}_5\text{I}_2$ was also highly dependent on the N_2 adsorption and demonstrated the proposed mechanism of molecular oxygen activation over $\text{Bi}_4\text{O}_5\text{I}_2\text{-OV}$ possessed good commonality during the photocatalytic process. More importantly, it would broaden the application range of $\text{Bi}_4\text{O}_5\text{I}_2\text{-OV}$ photocatalyst and provide theory basis and directional guide for optimization design of highly efficient photocatalysts.

4. Conclusions

In summary, the oxygen vacancies were successfully introduced on $(10\bar{1})$ facets of bismuth-rich $\text{Bi}_4\text{O}_5\text{I}_2$ ($\text{Bi}_4\text{O}_5\text{I}_2\text{-OV}$) by a facial solvothermal method. According to the DFT calculations, the incorporation of oxygen vacancies could strengthen the O_2 absorption. In

addition, the enhanced O_2 adsorption increased the CBM and VBM of $\text{Bi}_4\text{O}_5\text{I}_2$, which induced an instantaneous surface-bulk homojunction accompanied with a built-in field formed at the interface between $\text{Bi}_4\text{O}_5\text{I}_2\text{-OV}$ with O_2 adsorption ($\text{Bi}_4\text{O}_5\text{I}_2\text{-OV-O}_2$) and bulk $\text{Bi}_4\text{O}_5\text{I}_2$. This homojunction accelerated charge transfer across the interface and facilitating the carrier separation. Thus $\text{Bi}_4\text{O}_5\text{I}_2\text{-OV}$ exhibited the best activity for molecular oxygen activation and the performance deteriorated gradually with the decrease of oxygen vacancies concentration. Consistent with molecular oxygen activation, $\text{Bi}_4\text{O}_5\text{I}_2\text{-OV}$ showed much enhanced activity of N_2 fixation, which reflected the good commonality of proposed mechanism. These findings may open new avenues towards the mechanistic understanding of the photocatalysts with surface vacancies and the design of high performance of $\text{Bi}_x\text{O}_y\text{I}_z$ based photocatalysts.

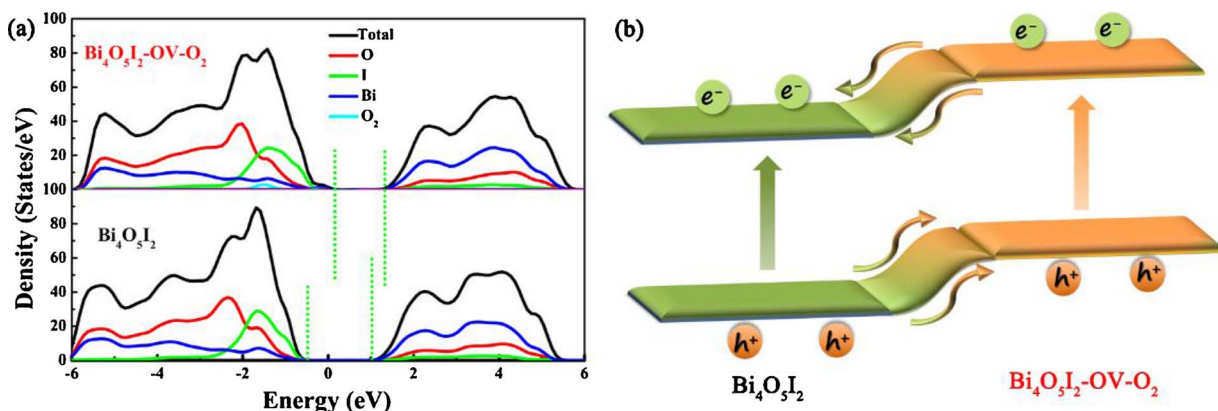


Fig. 7. Total DOS and partial DOS of bulk $\text{Bi}_4\text{O}_5\text{I}_2$ and surface of $\text{Bi}_4\text{O}_5\text{I}_2\text{-OV}$ with O_2 adsorption (a) and the illustration of charge transfer in the homojunction (b).

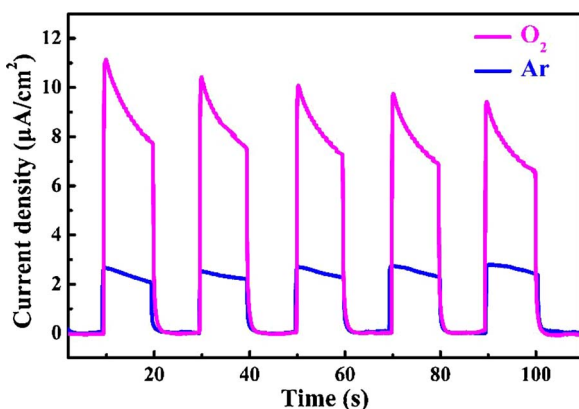


Fig. 8. Photocurrent responses of $\text{Bi}_4\text{O}_5\text{I}_2$ -OV- O_2 and $\text{Bi}_4\text{O}_5\text{I}_2$ -OV-Ar.

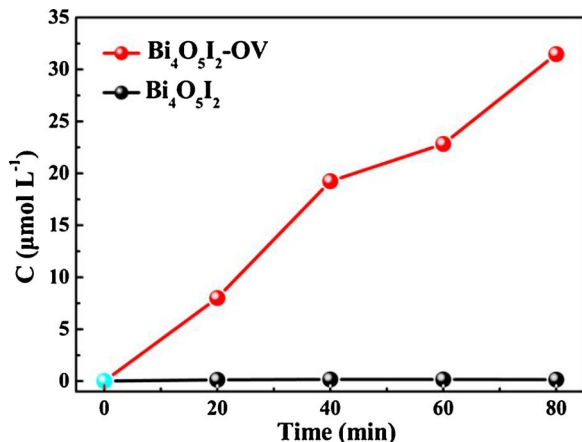


Fig. 9. The generated ammonia concentrations of the as-prepared $\text{Bi}_4\text{O}_5\text{I}_2$ -OV and $\text{Bi}_4\text{O}_5\text{I}_2$ at different irradiation time under visible light irradiation.

Acknowledgements

This work was financially supported by the National Nature Science Foundation of China (21471040 and 21303030).

Appendix A. Supplementary data

Supplementary data associated with this article can be found, in the online version, at <https://doi.org/10.1016/j.apcatb.2017.12.008>.

References

- [1] M. Metz, E.I. Solomon, J. Am. Chem. Soc. 123 (2001) 4938–4950.
- [2] A. Linsebigler, G. Lu, J. Yates Jr., Chem. Rev. 95 (1995) 735–758.
- [3] L. Khachaturyan, E. Vejerano, S. Lomnicki, B. Dellinger, Environ. Sci. Technol. 45 (2011) 8559–8566.
- [4] S.J. Tan, Y.F. Ji, Y. Zhao, A.D. Zhao, B. Wang, J.L. Yang, J.G. Hou, J. Am. Chem. Soc. 133 (2011) 2002–2009.
- [5] M.A. Henderson, I. Lyubinetsky, Chem. Rev. 113 (2013) 4428–4455.
- [6] C.C. Chen, W.H. Ma, J.C. Zhao, Chem. Soc. Rev. 39 (2010) 4206–4219.
- [7] Y.B. Zhao, W.H. Ma, Y. Li, H.W. Ji, C.C. Chen, H.Y. Zhu, J.C. Zhao, Angew. Chem. Int. Ed. 124 (2012) 3242–3246.
- [8] H. Sheng, H.W. Ji, W.H. Ma, C.C. Chen, J.C. Zhao, Angew. Chem. Int. Ed. 125 (2013) 9868–9872.
- [9] Y. Li, W. Zhang, J.F. Niu, Y.S. Chen, ACS Nano 6 (2012) 5164–5173.
- [10] E. Wahlström, E.K. Vestergaard, R. Schaub, A. Rønnaug, M. Vestergaard, E. Lægsgaard, I. Stensgaard, F. Besenbacher, Science 303 (2004) 511–513.
- [11] Y.B. He, A. Tilocca, O. Dulub, A. Selloni, U. Diebold, Nat. Mater. 8 (2009) 585–589.
- [12] A.L. Linsebigler, G.Q. Lu, J.T. Yates Jr., Chem. Rev. 95 (1995) 735–758.
- [13] M.D. Rasmussen, L.M. Molina, B. Hammer, J. Chem. Phys. 120 (2004) 988–997.
- [14] S. Tan, Y. Ji, Y. Zhao, A. Wang, B. Yang, J. Yang, J.G. Hou, J. Am. Chem. Soc. 133 (2011) 2002–2009.
- [15] N. Zhang, X. Li, H. Ye, S. Chen, H. Ju, D. Liu, Y. Lin, W. Ye, C. Wang, Q. Xu, J. Zhu, L. Song, J. Jiang, Y. Xiong, J. Am. Chem. Soc. 138 (2016) 8928–8935.
- [16] M. Kong, Y.Z. Li, X. Chen, T.T. Tian, P.F. Fang, F. Zheng, X.J. Zhao, J. Am. Chem. Soc. 133 (2011) 16414–16417.
- [17] H. Wang, S.C. Chen, D.Y. Yong, X.D. Zhang, S. Li, W. Shao, X.S. Sun, B.C. Pan, Y. Xie, J. Am. Chem. Soc. 139 (2017) 4737–4742.
- [18] L. Ye, K. Deng, F. Xu, L. Tian, T. Peng, L. Zan, Phys. Chem. Chem. Phys. 14 (2012) 82–85.
- [19] Y. Bai, T. Chen, P. Wang, L. Wang, L. Ye, Chem. Eng. J. 304 (2016) 454–460.
- [20] P. Cui, J. Wang, Z. Wang, J. Chen, X. Xing, L. Wang, R. Yu, Nano Res. 9 (2016) 593–601.
- [21] Y. Myung, F. Wu, S. Banerjee, A. Stoica, H. Zhong, S.S. Lee, J. Fortner, L. Yang, P. Banerjee, Chem. Mater. 27 (2015) 7710–7718.
- [22] D. Mao, S. Ding, L. Meng, Y. Dai, C. Sun, S. Yang, H. He, Appl. Catal. B: Environ. 207 (2017) 153–165.
- [23] X. Xiao, C.L. Xing, G.P. He, X.X. Zuo, J.M. Nan, L.S. Wang, Appl. Catal. B Environ. 148–149 (2014) 154–163.
- [24] X. Jin, L. Ye, H. Xie, G. Chen, Coord. Chem. Rev. 349 (2017) 84–101.
- [25] C.Y. Wang, X. Zhang, H.B. Qiu, W.K. Wang, G.X. Huang, J. Jiang, H.Q. Yu, Appl. Catal. B: Environ. 200 (2017) 659–665.
- [26] J. Shang, W.C. Hao, X.J. Lv, T.M. Wang, X.L. Wang, Y. Du, S.X. Dou, T.F. Xie, D.J. Wang, J.O. Wang, ACS Catal. 4 (2014) 954–961.
- [27] X. Jin, L. Ye, H. Wang, Y. Su, H. Xie, Z. Zhong, H. Zhang, Appl. Catal. B: Environ. 165 (2015) 668–675.
- [28] J. Wang, Y. Yu, L. Zhang, Appl. Catal. B: Environ. 136–137 (2013) 112–121.
- [29] Y. Su, C. Ding, Y. Dang, H. Wang, L. Ye, X. Jin, H. Xie, C. Liu, Appl. Surf. Sci. 346 (2015) 311–316.
- [30] X.J. Wang, Y. Zhao, F.T. Li, L.J. Dou, Y.P. Li, J. Zhao, Y.J. Hao, Sci. Rep. 6 (2016) 24918.
- [31] Y. Bai, L.Q. Ye, T. Chen, L. Wang, X. Shi, X. Zhang, D. Chen, ACS Appl. Mater. Interfaces 8 (2016) 27661–27668.
- [32] J.P. Perdew, K. Burke, M. Ernzerhof, Phys. Rev. Lett. 77 (1996) 3865–3868.
- [33] P.E. Blöchl, Phys. Rev. B 50 (1994) 17953–17979.
- [34] G. Kresse, D. Joubert, Phys. Rev. B 59 (1999) 1758–1775.
- [35] H. Li, J. Shi, K. Zhao, L. Zhang, Nanoscale 6 (2014) 14168–14173.
- [36] E. Keller, M. Krämer, H. -Schmidt, Z. Kristallogr., Zeitschrift für Kristallographie-Crystalline Materials 217 (2002) 256–264.
- [37] Y. Bai, L. Ye, T. Chen, P. Wang, L. Wang, X. Shi, P. Wong, Appl. Catal. B: Environ. 203 (2017) 633–640.
- [38] X. Xiao, C. Xing, G. He, X. Zuo, J. Nan, L. Wang, Appl. Catal. B: Environ. 148 (2014) 154–163.
- [39] H. Li, J. Shang, Z.H. Ai, L.Z. Zhang, J. Am. Chem. Soc. 137 (2015) 6393–6399.
- [40] Y.H. Lv, Y.F. Liu, Y.Y. Zhu, Y.F. Zhu, J. Mater. Chem. A 2 (2014) 1174–1182.
- [41] W. Kim, M. Choi, K. Yong, Sens. Actuators B 209 (2015) 989–996.
- [42] X.Y. Kong, Y.Y. Choo, S.P. Chai, A.K. Soh, A.R. Mohamed, Chem. Commun. 52 (2016) 14242–14245.
- [43] D.A. Panayotov, J.R. Morris, J. Phys. Chem. C 113 (2009) 15684–15691.
- [44] Y.B. Zhao, W.H. Ma, Y. Li, H.W. Ji, C.C. Chen, H.Y. Zhu, J.C. Zhao, Angew. Chem. Int. Ed. 124 (2012) 3242–3246.
- [45] G. Liu, G. Zhao, W. Zhou, Y. Liu, H. Pang, H. Zhang, D. Hao, X. Meng, P. Li, T. Kako, J. Ye, Adv. Funct. Mater. 26 (2016) 6822–6829.
- [46] A. Vittadini, A. Selloni, F.P. Rotzinger, M. Grätzel, Phys. Rev. Lett. 81 (1998) 2954–2957.
- [47] P. Li, Y. Zhou, Z. Zhao, Q. Xu, X. Wang, M. Xiao, Z. Zou, J. Am. Chem. Soc. 137 (2015) 9547–9550.
- [48] X. Wang, Q. Xu, M. Li, S. Shen, X. Wang, Y. Wang, Z. Feng, J. Shi, H. Han, C. Li, Angew. Chem. Int. Ed. 51 (2012) 13089–13092.
- [49] H. Li, J. Shang, Z.H. Ai, L.Z. Zhang, J. Am. Chem. Soc. 137 (2015) 6393–6399.